Percolation-Continuum Model of Evaporative Drying: Homogeneous or Patchy Saturation?

H. F. Wang, T. E. Strand, J. G. Berryman

February 25, 2005

Disclaimer

Percolation-Continuum Model of Evaporative Drying: Homogeneous or Patchy Saturation?

H. F. Wang and T. E. Strand

University of Wisconsin-Madison, Madison, Wisconsin

J. G. Berryman

University of California, Lawrence Livermore National Laboratory, Livermore, California

Porous rock on the earth's surface often contains more than one fluid phase, and an important case is partial saturation with air and water. We implemented a pore-scale, percolation model coupled with a continuum model for water vapor diffusion in order to create a simulated tomographic image of water distribution within a rock core during drying. As drying proceeds, the initial, continuous water cluster breaks up into smaller and smaller clusters with an increasing surface-area-to-volume ratio. Drying times are a function of the number and location of boundary surfaces, but the surface-area-to-volume ratio is approximately the same for a given saturation. By applying a Voigt volume average of the elastic properties of water-filled and air-filled cells, and by introducing the *ad hoc* rule that water-filled pores on the air-water interface of a cluster behave in a drained manner, we find elastic moduli as a function of saturation that mimic laboratory experimental data.

INTRODUCTION

The earth's crust near the surface consists of porous rock containing various liquids and gases, such as air, water, and hydrocarbons. When two or more fluids are present simultaneously, it is of significant practical interest to determine the amount and distribution of the phases from geophysical methods. Because probing the earth with elastic wave velocities is done extensively in oil and gas exploration and in environmental applications, interpreting geophysical measurements requires solving the inverse problem and hence knowledge of how elastic properties vary over a wide range of frequencies in rocks containing two fluid phases. An important case is partial saturation in which one phase is air and the other is water. Numerous models and measurements have been made for this case [*White*, 1975; *Dutta and Odé*, 1979a, b; *Murphy*, 1984; *Berryman et al.*, 1988; *Endres and Knight*, 1989; *Goertz and Knight*, 1988; *Mavko and Nolen-Hoeksema*, 1994; *Cadoret et al.*, 1995, 1988; *Dvorkin and Nur*, 1998; *Mavko and Mukerji*, 1998; *Knight et al.*, 1998; *Johnson*, 2001; *Tserkovnyak and Johnson*, 2002]. As discussed by *Berryman et al.* [2002], a central issue in dealing with the experimental results for partially saturated rocks at higher frequencies (sonic and ultrasonic) is that they can deviate significantly from what is predicted by the well-known Gassmann low-frequency (seismic) fluid-substitution theory. One explanation for deviations is that the saturation is patchy, *viz.*, some pores are filled entirely with water, whereas others are filled entirely with air. High-frequency stress variations induce differential pore pressures, which do not relax. At very low frequencies, water-filled regions have an adequate opportunity to relax during half a stress cycle, and consequently the overall behavior is the same as

the drained case. Drained behavior is equivalent to each pore containing the same mix of air and water, which has essentially the compressibility of air. Thus the very-low-frequency case is equivalent to fluids being homogeneously mixed, and the bulk and shear moduli can be predicted using the Gassmann formulation. Frequency of applied stress, the size distribution of the water clusters, and the hydraulic diffusivity of the porous medium are intertwined in the question "what is patchiness," in terms of elastic response. *Berryman and Pride* [2002, 2004] examined torsional waves in a partially saturated cylinder. Patchy saturation during drying was represented by a two-layer model in which the inner cylinder was completely saturated and the outer annulus was completely dry. Somewhat surprisingly, the patchy cylinder fits shear velocity data for Massillon sandstone at 560 Hz better than the Gassmann prediction, in which the only variation resulted from density changes.

Experimental, elastic modulus data at high frequency in partially-saturated rock span the range between homogeneous and patchy behavior [e.g., *Murphy*, 1984; *Knight and Nolen-Hoeksema*, 1990]. Because the water distribution is dependent upon saturation history, every process that produces changes in water saturation, e.g., evaporative drying, immiscible drainage, or imbibition, produces distinctive distributions of water-cluster sizes as a function of saturation. Although computed tomography techniques exist to examine fluid distributions in rocks, such images and associated elastic properties are not available. On the other hand, simulated images can be made for evaporative drying, which is the process by which different saturations are often achieved while elastic wave velocities are measured. Evaporative drying occurs in a variety of earth-science contexts — from the behavior of a nuclear waste repository in the unsaturated zone, to laboratory studies for determining how elastic wave velocities vary with water. In common with other drainage processes which involve competition among forces of gravity, capillarity, and pressure, the pore-level detail of water distribution cannot be obtained using continuum models based on averaging over an REV. This paper presents results for evaporative drying of laboratory-sized rectangular parallelepipeds using a combined percolation (water phase) and continuum (air phase) model [*Prat*, 1993, 2002]. Several permutations of open and closed boundary surfaces are employed. In addition, simulations are performed for different Bond numbers (ratio of gravity to capillary forces). These simulations are examined qualitatively and quantitatively in terms of the nature of the drying front and the distribution of water-cluster-size changes as drying occurs. The results are then examined for estimating elastic moduli.

DRYING MODEL

To quantify the saturation distribution during drying, we implemented a computational model to simulate the process at the pore scale. A complete description of the modified invasion percolation (MIP) and drying model is given by *Strand* [2003]. As indicated in the introduction, the drying model builds upon Prat's coupled percolation-continuum approach, which properly captures the two-phase flow and diffusion aspects of the problem. Drying involves the slow displacement of air into a water-saturated porous meduim. The MIP model includes capillary and buoyancy forces exclusively because viscous forces are assumed negligible. In the basic MIP model, the porous medium is represented statistically on a three-dimensional lattice. The lattice periodicity is determined by the mean grain size $\langle R_g \rangle$. Two different distribution functions are used to represent the nonwetting radii R_{nw} (throats) and wetting radii R_w (pores). The nonwetting radius is the minimum radius of curvature on the grain scale and provides the maximum local resistance to drainage, whereas the wetting radius is the maximum radius of curvature and provides the maximum local resistance to imbibition. The wetting radii are the pores, which are the sites of the lattice; and the nonwetting radii are the throats, which are the bonds of the lattice emanating from the sites with coordination number Z_c representing the average number of connections at sites. The terminology of wetting and nonwetting fluid radius distributions is preferred over the pore/throat terminology primarily to avoid the implications of an assumed and regular geometry that is often associated with pores/throats. By referencing the two distinct length scale distributions according to wetting and nonwetting fluids, it is inferred that they must be measured by means of displacement experiments. These length scales represent intrinsic properties of the pore space geometry, but it must be noted that they are effective, as opposed to actual, lengths. The implementation of percolation models for simulating immiscible displacement involves the definition of a pore-filling potential at each location on the interface [*Larson et al.*, 1981; *Wilkinson*, 1984; *Meakin et*

al., 1992; *Ioannidis and Chatzis*, 1993; *Chaouche et al.*, 1994; *Glass and Yarrington*, 1996; *Glass et al.*, 1998, 2001; *Xu et al.*, 1998]. The physics are incorporated through a percolation parameter, Ψ_i, which is a measure of the probability of invasion at all interface sites i. The percolation parameter incorporates the physical forces of buoyancy and capillary pressures, $P_{b,i}$ and $P_{c,i}$ respectively, where

$$P_{b,i} = \Delta\rho g h_i = \Delta\rho g 2\langle R_g\rangle H_i \tag{1}$$

and

$$P_{c,i} = \frac{2\gamma}{R_{nw,i}} \tag{2}$$

where $\Delta\rho$ is the density contrast between the two fluid phases (essentially ρ_w, water density when air is the gas phase), h_i is the height of site i relative to a datum, $H_i = h_i/(2\langle R_g\rangle)$ is a normalized height, and γ is the interfacial tension. The mean capillary pressure can be normalized

$$\bar{P}_c = \frac{2\gamma}{\langle R_{nw}\rangle}, \tag{3}$$

and the nonwetting Bond number can be defined as

$$Bo_{nw} = \frac{\Delta\rho g\langle R_g\rangle\langle R_{nw}\rangle}{\gamma}. \tag{4}$$

Note that the Bond number is a nondimensional ratio of gravity to capillary forces. These two steps lead to the definition of the percolation parameter,

$$\Psi_i = Bo_{nw}H_i - \frac{\langle R_{nw}\rangle}{R_{nw,i}}. \tag{5}$$

The MIP model proceeds by invading the location on the interface that maximizes Equation 5 at each time step. Each invasion step involves the penetration of the identified nonwetting fluid radius, where the meniscus enters a region of increasing cross-sectional area. The resulting pressure imbalance leads to rapid filling of the adjacent pore (wetting fluid radius) and exposes a new set of nonwetting fluid radii. The interface list is updated accordingly, and another time step is performed until the termination criterion $\max(\Psi_i) \leq 0$ is met. Expressed differently, air invasion continues as long as gravitational forces associated with the suspended water column exceed the minimum local (threshold) capillary force on the interface.

The drying model involves several modifications of the MIP model:

1. *Incorporating clustering of the water phase:* As air invades the porous medium, the defending water phase is broken into numerous disconnected clusters. This process is analogous to the trapping of the defending phase. However, because evaporation occurs at every part of the air-water interface, the isolated clusters must be allowed to continue to be invaded by air. Because clusters remain eligible for invasion in the drying model, identifying them required adjusting the data structures to improve efficiency. The simplest way to identify a new isolated cluster is to do a connectivity search by examining every water-filled site in the lattice. This must be accomplished through a series of nearest neighbor searches and has a time complexity $O(L^3)$ at each invasion step. An improved method has been implemented that has time complexity $O(constant)$, where the constant is on the order of the maximum cluster size (which does not scale with the system size but is dependent on the buoyancy Bond number). This method involves a parallel search of all water sites adjacent to the most recently invaded site.

2. *Allowing independent percolation events at each cluster:* The percolation (air invasion) events at each cluster are independent of the other clusters (though coupled temporally via the continuum model). Each cluster therefore represents a separate list of possible invasion locations. Once a cluster has been identified as the next to host an invasion step, the appropriate throat is chosen as described by the MIP model from that cluster's list of interface throats. Invasion occurs as usual, and the interface list is updated, generating additional clusters if necessary.

3. *Coordinating percolation events among clusters by temporal sequencing:* Once the clusters have been identified and the percolation events isolated among them, the drying model must coordinate the invasion steps by attributing an evaporation rate to each cluster and independently tracking the progression of time. A percolation event occurs each time a cluster loses a pore volume V_{pore} of water. Upon formation, each cluster is assigned a state variable, the incremental fluid volume, V_{inc}, which is initially set equal to V_{pore}. The

cluster evaporation rate and incremental volume yield a time to invasion for each cluster. The cluster with the minimum invasion time is the next to host a percolation event, time is updated by the appropriate amount Δt, the incremental volume of each cluster is reduced using Δt and the respective evaporation rate, and V_{inc} for the invaded cluster is reset to V_{pore}. The incremental volume of each cluster is updated based on the time to the percolation event and its evaporation rate. This process is repeated for each invasion step.

4. *Coupling between evaporation at each cluster and water vapor diffusion in the air phase:* At each time step, the continuum model solves for the steady-state water-mass fraction in the air phase. This is accomplished using an iterative relaxation method that updates the mass fraction using the total mass flow out of each pore i:

$$\dot{M}_{wi} = \sum_j \dot{m}_{wij} \qquad (6)$$

where $\dot{m}_{wij}$ is the mass flow rate between pore i and pore j. The system is solved when $\dot{M}_{wi} = 0$ at all pores i. Computationally, this corresponds to continuing to iterate as long as the cumulative residual is greater than some threshold ϵ, where the residual δ_{cum} is given by

$$\delta_{cum} = \sqrt{\sum_i (\dot{M}_{wi})^2} \,. \qquad (7)$$

Because the continuum model increases in size by one pore at each time step, the threshold ϵ is taken to be proportional to the number of percolation steps (air-filled pores).

To this point, the continuum model gives the steady-state water concentration in each air-filled pore, and the percolation model tracks the formation of, monitors the respective interface areas of, and allows independent percolation events on, each water cluster. The final step in implementing the model involves using the state of the continuum model to determine the evaporation rate of each cluster. A percolation event occurs on a particular cluster each time that cluster loses a pore volume, V_{pore}, of fluid.

To summarize, the coupled percolation-continuum drying algorithm begins with a water-saturated porous medium of prescribed system size, pore space statistics, and boundary conditions. Initially, there is a single cluster with the air-water interface at the open boundaries (or boundary), and the remaining boundaries utilize no-flow conditions. All open faces are subject to ambient conditions (zero water content, ambient temperature) across the boundary. Given this initial state, the following algorithm at each time step is performed until the liquid water has been fully (or sufficiently) evaporated from the system:

1. Individual water clusters are identified.

2. The largest nonwetting radius at the air-water interface of each cluster is invaded. The percolation events in each water cluster are treated independently. Air invasion occurs as long as gravitational force exceeds the minimum capillary force on the interface.

3. The evaporation flux is calculated at the boundary of each cluster.

4. The diffusion model is coupled with the percolation model by invading the cluster that loses a pore volume due to evaporation. Percolation events are temporally sequenced among water clusters. Water vapor diffusion in the air phase means that there are no trapped clusters.

DRYING SIMULATION RESULTS

Simulated Tomographic Images

The parameters used in our simulations were based on the following values. A mean grain size $\langle R_g \rangle$ was chosen in the range 0.05 to 0.6 mm. The mean pore size $\langle R_w \rangle$ was chosen to be $0.4\langle R_g \rangle$, which corresponds to a porosity of about 6.4%. The mean throat size $\langle R_{nw} \rangle$ was chosen to be $0.2\langle R_w \rangle$. Standard deviations of the two distributions were 0.15 of the mean. This section contains visualizations of the rock core during drying for three different sets of open surfaces (Figures 1-3): only the top surface is open, all sides are open with the top and bottom closed, only the bottom surface is open. More extensive graphical results are presented in *Strand* [2003]. In Figures 1-3 each panel represents a vertical cross section of the initially 100% water-saturated sample. Each horizontal row depicts the water-air distribution at a given saturation calculated as a volume average over the entire sample. In

the bitmap images, black represents a water-filled cell and white represents an air-filled cell.

Top Open: In the case in which all the boundaries are closed except for the top, evaporation occurs as a relatively flat drying front moving from the top to the bottom of the core. As the front moves downward, the water-saturated part of the medium is broken into myriad clusters of water. These water clusters begin to shrink and eventually evaporate completely, leaving an air-saturated region above the traveling front. For clusters farther away from the water-saturated region, the concentration of water vapor in the air surrounding the cluster is continually decreasing. This causes the mass flux in each interface throat to increase, along with the cluster evaporation rate (normalized by surface area). Water clusters are therefore limited in their distance beyond the water-saturated region before complete evaporation, causing a band of air phase to form at the top of the core and grow downward during evaporation.

Sides Open: In the case in which the top and bottom boundaries are closed but all lateral boundaries are open, a region of high air saturation quickly forms beneath the top boundary and, as before, an initial horizontal drying front moves downward. The early character of the main (zeroth order) water cluster is more rounded in the center as opposed to being relatively flat, reflecting the fact that air must invade from the lateral boundaries to form the upper air region. As the drying front moves downward, small water clusters extend all the way to the top boundary, even at very low water saturation, because the closed top boundary prevents the formation of strong vertical gradients in the water-vapor concentration of the air phase.

Bottom Open: The case in which the bottom boundary is open and all other boundaries are closed corresponds to one of the cases considered in the experiments and simulations of *Prat* [1993; 2002], and our observations are essentially the same as reported therein. Namely, drying initiates with a single finger of air forming at the bottom face and migrating to the top of the core. The finger is relatively narrow and does not intersect the plane shown in Figure 3, but it can be seen in other views. The finger acts as a conduit for air and allows the formation of a region of high air saturation at the top of the core. A horizontal drying front forms and migrates downward, as observed in previous cases. Relatively small clusters of water form behind the front and remain uniformly distributed and essentially constant in size until the bottom boundary is reached because all evaporation takes place at the bottom face. Water vapor concentrations in the air phase remain close to the saturated value because only the single finger connects the upper air region to the dry air outside. Gradients remain very small, and the clusters evaporate very slowly. Once the initial drying front reaches the bottom face, a secondary drying front forms at the bottom face and migrates upward, eliminating the disconnected clusters, and strong vertical gradients in the water vapor concentration are now present.

For all three cases, drying can be viewed as a two-stage sequence. In the first stage, the initial, single water cluster breaks into many as the drying front moves downward. The drying front for the case of an open top is relatively flatter. The secondary drying front moves inward from all open sides, progressively eliminating residual water clusters. The spatial location of residual water clusters depends significantly on the boundary conditions. The air-saturated region occupies the space between the residual water clusters and the open surfaces. The sizes and distribution of residual water clusters are highly dependent on the applied boundary conditions. When only the top face is open, residual clusters are limited to a narrow band along the initial drying front, and the secondary drying front is nearly eliminated. In contrast, when other faces are open (top open or closed), residual water clusters are larger in size and are more widely distributed, and the secondary drying front can be clearly observed moving inward from all open faces.

Effect of Varying Grain Size

This subsection examines the effects of varying the grain size while holding the physical dimensions of the system constant at $2 \text{ cm} \times 2 \text{ cm} \times 3 \text{ cm}$. The ratios $\langle R_w \rangle / \langle R_g \rangle$ and $\langle R_{nw} \rangle / \langle R_w \rangle$ are kept constant; thus, the porosity remains constant. Because the nonwetting throat radius $\langle R_{nw} \rangle$ is proportional to mean grain radius, the change in Bond number is proportional to the square of $\langle R_g \rangle$. As the grain size is varied between 0.05 mm and 0.6 mm, the Bond number changes between 9.54×10^{-5} and 1.37×10^{-2}. The results of the MIP model can be interpreted to be the same for the same Bond number as long as the other parameters are scaled appropriately. The coupled MIP-continuum drying model is expected to show qualitatively similar water-cluster configurations for the same Bond

number because the sequencing of the air invasion is governed principally by the percolation model. Other aspects of the model, such as the drying rate and vapor concentrations, would not be expected to depend only on Bond number. Figure 4 shows water clusters and vapor concentration profiles in the $x = 0$ plane as water saturation decreases from 80% (top row) to 3.3% (bottom row) and grain size decreases to the right. The size of the largest generated clusters remains close to constant as the grain size decreases, although there is an extensive increase in the production of smaller water clusters.

One measure of the size distribution of water clusters is the fraction of the water-filled cells that reside at the air-water interface, f_i, shown as a function of water saturation for different grain sizes (Figure 5):

$$f_i = \frac{n_{\text{interface}}}{n_{\text{wet}}}, \tag{8}$$

where $n_{\text{interface}}$ is the number of water-filled cells at the air-water interface and n_{wet} is the total number of water-filled cells. Although the results are given only for the case of the top surface being open, simulations showed that the fraction of cells at the water-air interface, for a given grain size and saturation, is fairly independent of boundary conditions, even though contours of saturation distribution within the rock sample can be quite different. The drying process appears to produce similar cluster sizes at different saturations. In other words, the functional form of the fraction of water-filled cells on the interface depends primarily on water saturation, and f_i is larger at a given water saturation S_w for decreasing grain size, and hence, Bond number (i.e. relatively greater capillarity). For the smallest grain size, over 90% of water-filled cells are at the air-water interface for water saturations between 0% and 40%. For the largest grain size, the percentage of water-filled cells at the interface decreases rapidly over the same water saturation range so that most of the water resides in the interior of the clusters. Thus, for a given water saturation, water tends toward larger clusters and can be characterized as "patchier" for larger grain sizes.

LAMÉ PARAMETER (λ) PLOTS

Before presenting the elastic moduli simulation results, we must explain why they are presented in terms of the ratio λ/μ, where λ is Lamé's parameter and μ is shear modulus [*Berryman et al.*, 2002]. Because μ is generally independent of saturation, most of the variation of the ratio is to be expected

to be in λ. Based on the standard relations between elastic wave velocities and elastic moduli, the ratio λ/μ is related to the square of the V_p/V_s ratio:

$$\frac{\lambda}{\mu} = \left(\frac{V_p}{V_s}\right)^2 - 2 . \tag{9}$$

Berryman et al. [2002] examined how the phase distribution of gas and liquid influences the ratio λ/μ as a function of saturation and frequency. If the gas and liquid are homogeneously mixed, then the dry or drained value is expected for water saturations between 0% and approximately 95%. The ratio increases rapidly to the undrained value between 95% and 100%. Dry or drained response is expected also at frequencies low enough to satisfy the Gassmann assumption of drained behavior when the liquid is patchily distributed, that is, when gas and liquid are segregated with some patches containing only gas while other patches contain only liquid. If, on the other hand, the liquid is patchily distributed and the measurement frequency is higher such that no pore pressure equilibration occurs, then the Gassmann equation for undrained response applies locally, and the macroscopic response is a volume (Voigt) average of the individual liquid-filled and gas-filled regions. The Voigt average associated with these assumptions for patchy saturation is a linear function of saturation, ranging from the drained value at zero water saturation to the undrained value at full saturation. Because the measured field or laboratory values of λ/μ depend on the exact nature of the liquid phase geometry and the frequency, they can only be expected to fit within a bounding triangle whose base is the dry or drained value and whose hypotenuse $(\lambda/\mu)^{\text{Voigt}}$ connects drained and undrained values (Figure 6). Laboratory data at higher frequencies typically plot within the triangle indicating behavior intermediate between homogeneous and patchy.

ELASTIC-WAVE VELOCITY SIMULATION RESULTS

The distribution of water clusters obtained from the drying simulations is used to estimate elastic moduli. The computational model is based on a critical assumption that pores containing water on the two-phase interface as well as air-filled cells behave in a drained manner. This assumption breaks the simple linear relationship between elastic moduli as a function of saturation, and it introduces a dependence on the size distribution of fluid-filled patches. Only strictly interior, water-filled cells

6

are assumed to behave in an undrained manner. For this model, the fraction of cells behaving in a drained manner is the sum of air-filled cells and water-filled cells at the water-air interface. Recall that f_i is the fraction of water-filled cells at the interface of a water cluster, and note that, for these simulations, the number of water-filled cells can be counted, as can the number of water-filled cells at the air-water interface. The number of drained (dry) *behaving* cells normalized by the total number N of cells in the sample is

$$\frac{{}^{\prime}n_{\text{dry}}{}^{\prime}}{N} = \frac{n_{\text{dry}}}{N} + f_i S_w \ , \tag{10}$$

and the number of undrained (wet) *behaving* cells as a function of the total sample volume is

$$\frac{{}^{\prime}n_{\text{wet}}{}^{\prime}}{N} = 1 - \frac{{}^{\prime}n_{\text{dry}}{}^{\prime}}{N} = \frac{n_{\text{wet}}}{N} - f_i S_w \ . \tag{11}$$

Explicitly also

$$\frac{n_{\text{dry}}}{N} = 1 - S_w \tag{12}$$

and

$$\frac{n_{\text{wet}}}{N} = S_w \ . \tag{13}$$

The effective elastic moduli are then computed as a function of S_w using a Voigt volume average of the "dry" and "wet" behaving fractions:

$$\frac{\lambda}{\mu} = \left(\frac{\lambda}{\mu}\right)^{\text{dry}} \frac{{}^{\prime}n_{\text{dry}}{}^{\prime}}{N} + \left(\frac{\lambda}{\mu}\right)^{\text{wet}} \frac{{}^{\prime}n_{\text{wet}}{}^{\prime}}{N} \ . \tag{14}$$

For the patchy saturation limit shown in Figure 6, we have

$$\left(\frac{\lambda}{\mu}\right)^{\text{Voigt}} = \left(\frac{\lambda}{\mu}\right)^{\text{dry}} \frac{n_{\text{dry}}}{N} + \left(\frac{\lambda}{\mu}\right)^{\text{wet}} \frac{n_{\text{wet}}}{N} \ , \tag{15}$$

which allows us to write Equation 14 as a correction to the patchy saturation limit:

$$\frac{\lambda}{\mu} = \left(\frac{\lambda}{\mu}\right)^{\text{Voigt}} + f_i S_w \left[\left(\frac{\lambda}{\mu}\right)^{\text{dry}} - \left(\frac{\lambda}{\mu}\right)^{\text{wet}}\right] \ . \tag{16}$$

The results shown in Figure 6 are based on the values of f_i shown in Figure 5. The numerical values used for the moduli were $\lambda^{\text{dry}} = 5\text{GPa}$, $\lambda^{\text{wet}} = 17\text{GPa}$, and $\mu^{\text{dry}} = \mu^{\text{wet}} = 12\text{GPa}$. All model results for different values of the Bond number fit within the bounding triangle defined by *Berryman et al.* [2002]. The trend is toward behavior that is more Gassmann-like for smaller grain sizes and

approaches pure patchy-saturation for larger grain sizes. The key determinant of elastic behavior is the size of water clusters. As shown in Figure 5, a greater fraction of cells is at the interface for smaller grain sizes. For example, 89.4% of water-filled cells are at the interface at an overall water saturation of 0.4 for a grain size of 0.05 mm, whereas only 25.1% of water-filled cells are at the interface for the same overall water saturation but for a grain size of 0.6 mm. The distribution of water clusters thus includes a relatively larger number of smaller water clusters at smaller grain size. As a result, essentially drained behavior is maintained for water saturations up to 0.4 for the smallest grain size. Conversely, larger water clusters, which have correspondingly fewer cells at the water-air interface, show behavior tending toward that of patchy saturation.

Although the model being presented is qualitative in nature, its conceptual basis is supported by the plots of λ/μ versus water saturation from experimental results (Figures 7-9). For example, both Massillon sandstone (23% porosity) and Spirit River sandstone (7.1% porosity) display approximately drained behavior between $S_w = 0$ and $S_w = 0.4$ at measurement frequencies of 200 kHz and 600 kHz, respectively, whereas Schuler-Cotton Valley sandstone (5.1% porosity) approaches the patchy saturation limit at 200 kHz [*Knight and Nolen-Hoeksema,* 1990; *Murphy,* 1984]. These comparisons demonstrate that the variation of Lamé's parameter with saturation at high frequency is compatible with percolation processes governing the distribution of water-cluster sizes during drying.

COMPARISON TO JOHNSON'S PATCHY-SATURATION THEORY

Johnson [2001] found the ratio of surface area of the water-air interface, to sample volume, S/V, to characterize the geometry of saturation patches as one of only two parameters required in an analytical model for the frequency dependence of the complex bulk modulus in partially saturated rock. In particular, S/V is proportional to the first-order correction term at high frequency, which lowers the bulk modulus from the Voigt average for pure patchy saturation. The factor $f_i S_w$ in the correction term of Equation 16, which results from applying a Voigt volume average of the elastic properties of water-filled and air-filled cells, plus the *ad hoc* rule that water-filled pores on the air-water interface of a

cluster behave in a drained manner, is also proportional to S/V:

$$f_i S_w = \frac{\langle R_g \rangle}{\phi} \left(\frac{S}{V} \right) \qquad (17)$$

where ϕ is the porosity, because $f_i S_w = (1/\phi)(n_{\text{interface}}/N)$, and $n_{\text{interface}} = S/\langle R_g \rangle^2$ and $N = V/\langle R_g \rangle^3$. Smaller Bond numbers (relatively higher capillary forces *vis a vis* gravity) lead to higher S/V, and hence, softer elastic behavior.

Johnson's second parameter $T \equiv l_f{}^2/D_T$ is the (complex) coefficient associated with the first-order expansion in frequency of the complex bulk modulus for very low frequencies. The parameter T is the mean time for diffusion across an effective fluid-patch size, l_f, and D_T is a diffusivity similar to that of a deformable skeletal frame in an incompressible, viscous fluid. Johnson defines the effective fluid-patch size as

$$l_f \equiv \frac{1}{V_f} \int_{V_f} \tilde{\Phi} d^3 \mathbf{r}, \qquad (18)$$

where the auxiliary function $\tilde{\Phi}$ satisfies Poisson's equation:

$$\nabla^2 \tilde{\Phi} = -1 \qquad (19)$$

within fluid patches and is zero outside. Thus, the quantity l_f can be obtained from a numerical, finite-difference solution using the cell-by-cell output of the drying model. In the future we anticipate using our drying model results to compute the entire frequency spectrum of the complex bulk modulus.

CONCLUSIONS

Our percolation-continuum model provides a simulated tomographic image of water distribution within a rock core during drying. The model gives a pore-scale, pictorial view of the nature of "patchy saturation." The distribution of water-cluster sizes is primarily a function of water saturation for different boundary conditions. In particular, the fraction of water-filled cells at the air-water interface, and hence the interface surface-area-to-sample-volume (S/V) ratio, is insensitive to which boundary surfaces are open to air. At a given water-saturation level, the (S/V) ratio increases as the average grain size decreases. Water at the phase interface is assumed to behave locally in a drained fashion, even at high frequency. This assumption yields elastic behavior as a function of saturation that approximates high-frequency measurements in several sandstones. In the model predictions, smaller

grain-size sandstones display Gassmann-like behavior at low water saturations, whereas sandstones consisting of larger grain size display nearly ideal patchy behavior. With the success of these simulations, Johnson's [2001] model can be applied to obtain the complete frequency dependence of the complex bulk modulus in partially saturated rock using our simulated water saturation distribution.

REFERENCES

[1] Berryman, J. G., and S. R. Pride, Dispersion of extensional and torsional waves in porous cylinders with patchy saturation, in *Proc. Second Biot Conference on Poromechanics,* Grenoble, France, edited by J.-L. Auriault, C. Geindreau, P. Royer, and J.-F. Bloch. pp. 613-618, A. A. Balkema, Rotterdam, 2002.

[2] Berryman, J. G., and S. R. Pride, Dispersion of waves in porous cylinders with patchy saturation Part I. Formulation and torsional waves, UCRL-JRNL-205634, 13 pp., 2004.

[3] Berryman, J. G., L. Thigpen, and R. C. Y. Chin, Bulk elastic wave propagation in partially saturated porous solids, *J. Acoust. Soc. Am., 84,* 360-373, 1988.

[4] Berryman, J. G., P. A. Berge, and B. P. Bonner, Estimating rock porosity and fluid saturation using only seismic velocities, *Geophysics, 67,* 391-404, 2002.

[5] Cadoret, T., D. Marion, and B. Zinszner, Influence of frequency and fluid distribution on elastic wave velocities in partially saturated limestones, *J. Geophys. Res., 100,* 9789-9803, 1995.

[6] Cadoret, T., G. Mavko, and B. Zinszner, Fluid distribution effect on sonic attenuation in partially saturated limestones, *Geophysics, 63,* 154-160, 1998.

[7] Chaouche, M., N. Rakotomalala, D. Salin, B. Xu, and Y. C. Yortsos, Invasion percolation in a hydrostatic or permeability gradient: Experiments and simulations, *Phys. Rev. E, 49(5),* 4133-4139, 1994.

[8] Dutta, N. C., and H. Odé, Attenuation and dispersion of compressional waves in fluid filled porous rocks with partial gas saturation (White model)– Part I: Biot theory, *Geophysics, 44,* 1777-1788, 1979a.

[9] Dutta, N. C., and H. Odé, Attenuation and dispersion of compressional waves in fluid filled porous rocks with partial gas saturation (White model)– Part II: Results, *Geophysics, 44,* 1789-1805, 1979b.

[10] Dvorkin, J., and A. Nur, Acoustic signatures of patchy saturation, *Internat. J. Solids Struct., 35,* 4803-4810, 1998.

[11] Endres, A. L., and R. Knight, The effect of microscopic fluid distribution on elastic wave velocities, *The Log Analyst, 30,* 437-444, 1989.

[12] Glass, R. J., and L. Yarrington, Simulation of gravity fingering in porous media using a modified invasion percolation model, *Geoderma, 70,* 231-252, 1996.

[13] Glass, R. J., M. J. Nicholl, and L. Yarrington, A modified invasion percolation model for low-capillary number immiscible displacements in horizontal rough-walled fractures: Influence of local in-plane curvature, *Water Resources Res., 34(12),* 3215-3234, 1998.

[14] Glass, R. J., S. H. Conrad, and L. Yarrington, Gravity-destabilized nonwetting phase invasion in macroheterogeneous porous media: Near pore-scale macro modified invasion percolation simulation of experiments, *Water Resources Res., 37(5),* 1197-1207, 2001.

[15] Goertz, D., and R. Knight, Elastic wave velocities during evaporative drying, *Geophysics, 63,* 171-183, 1998.

[16] Ioannidis, M. A., and I. Chatzis, Network modeling of pore structure and transport properties of porous media, *Chemical Eng. Science, 48,* 951-972, 1993.

[17] Johnson, D. L., Theory of frequency dependent acoustics in patchy-saturated porous media, *J. Acoust. Soc. Am., 110(2),* 682-694, 2001.

[18] Knight, R., and R. Nolen-Hoeksema, A laboratory study of the dependence of elastic wave velocities on pore scale fluid distribution, *Geophys. Rev. Lett., 17,* 1529-1532, 1990.

[19] Knight, R., J. Dvorkin, and A. Nur, Acoustic signatures of partial saturation, *Geophysics, 63,* 132-138, 1998.

[20] Larson, R. G., L. E. Scriven, and H. T. Davis, Percolation theory of two-phase flow in porous media, *Chemical Eng. Science, 36,* 57-73, 1981.

[21] Mavko, G., and D. Jizba, Estimating grain-scale fluid effects on velocity dispersion in rocks, *Geophysics, 56,* 1940-1949, 1991.

[22] Mavko, G., and T. Mukerji, Bounds on low-frequency seismic velocities in partially saturated rocks, *Geophysics, 63,* 918-924, 1998.

[23] Mavko, G., and R. Nolen-Hoeksema, Estimating seismic velocities in partially saturated rocks, *Geophysics, 59,* 252-258, 1994.

[24] Meakin, P., J. Feder, V. Frette, and T. Jossang, Invasion percolation in a destabilizing gradient, *Phys. Rev. A, 46(6),* 3357-3368, 1992.

[25] Murphy, W. F., III, Acoustic measures of partial gas saturation in tight sandstones, *J. Geophys. Res., 89,* 11549-11559, 1984.

[26] Prat, M., Percolation model of drying under isothermal conditions in porous media, *Int. J. Multiphase Flow, 19,* 691-704, 1993.

[27] Prat, M., Recent advances in pore-scale models for drying of porous media, *Chem. Eng. J., 86,* 153-164, 2002.

[28] Strand, T. E., Pore-scale Percolation Modeling of Two-Phase Flow in Granular Porous Media, Ph.D. Thesis, University of Wisconsin-Madison, 289 pp., 2003.

[29] Tserkovnyak, Y., and D. L. Johnson, Can one hear the shape of a saturation patch?, *Geophys. Res. Lett. 29,* 12, 2002.

[30] White, J. E., Computed seismic speeds and attenuation in rocks with partial gas saturation, *Geophysics, 40,* 224-232, 1975.

[31] Wilkinson, D., Percolation model of immiscible displacement in the presence of buoyancy forces, *Phys. Rev. A, 30,* 520-531, 1984.

[32] Xu, B., Y. C. Yortsos, and D. Salin, Invasion percolation with viscous forces, *Phys. Rev. E, 57(1),* 739-751, 1984.

J. G. Berryman, P. O. Box 808, L-200, Livermore, CA 94551-9900

T. E. Strand, TSI Incorporated, 500 Cardigan Road, Shoreview, MN 55126-3996

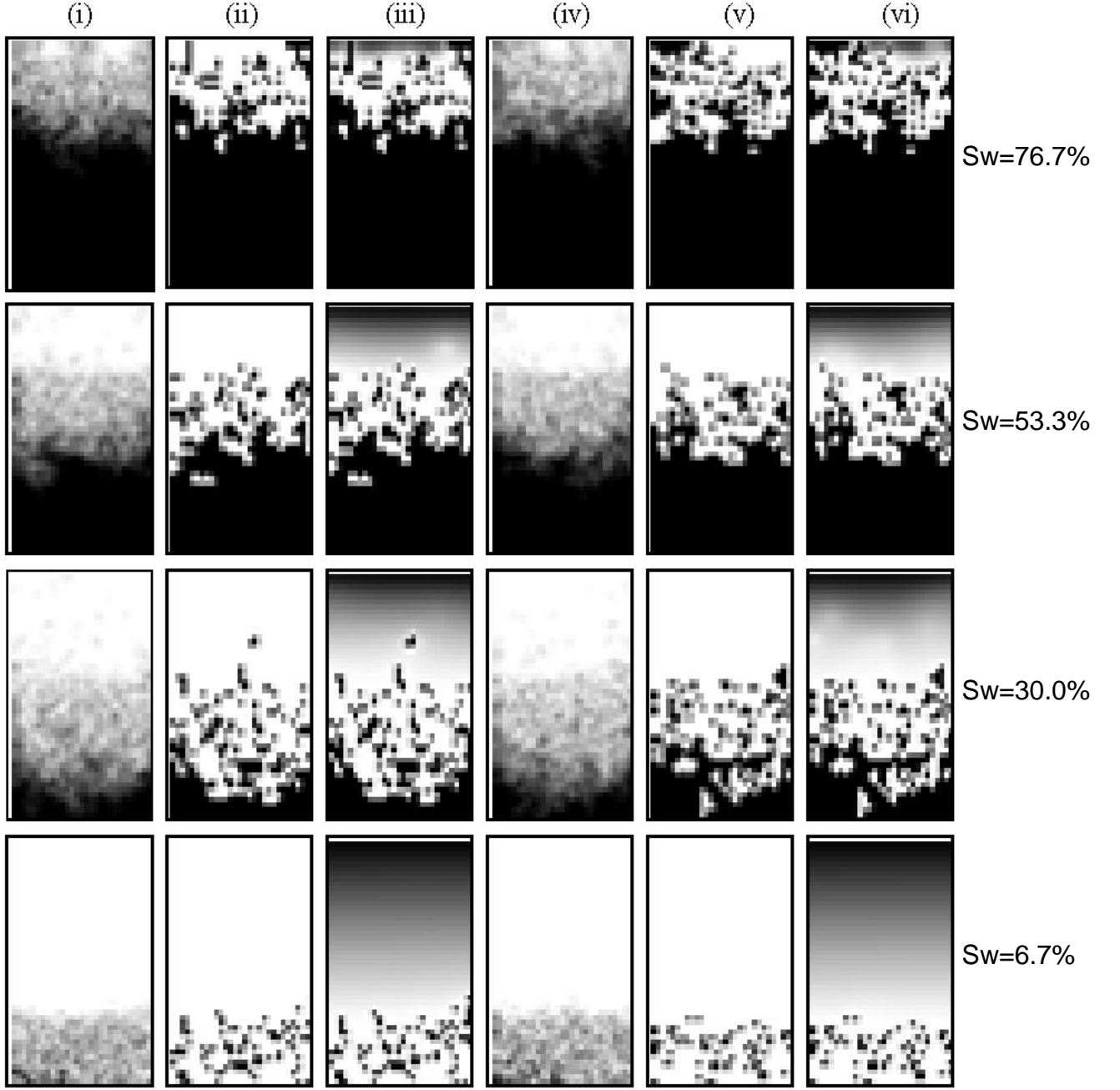H. F. Wang, Department of Geology and Geophysics, 1215 W. Dayton St., Madison, WI 53706

Figure 1: Drying model results for top surface open and all other surfaces closed. Each row from top to bottom represents water saturation values S_w of 76.7%, 53.3%, 30.0%, and 6.7%, respectively. First three columns from left to right are in the plane $x = 0$ showing, respectively: (i) Linear saturation averages, white $\leftrightarrow$ air, black $\leftrightarrow$ water, (ii) Phase distribution bitmap, white $\leftrightarrow$ air, black $\leftrightarrow$ water, (iii) Water vapor concentration in air phase, black $\leftrightarrow$ pure phase (air or water), grayscale indicates water vapor content (white $\leftrightarrow$ saturation vapor concentration). Remaining three columns (iv)-(vi) repeat the same quantities in the plane $y = 0$.
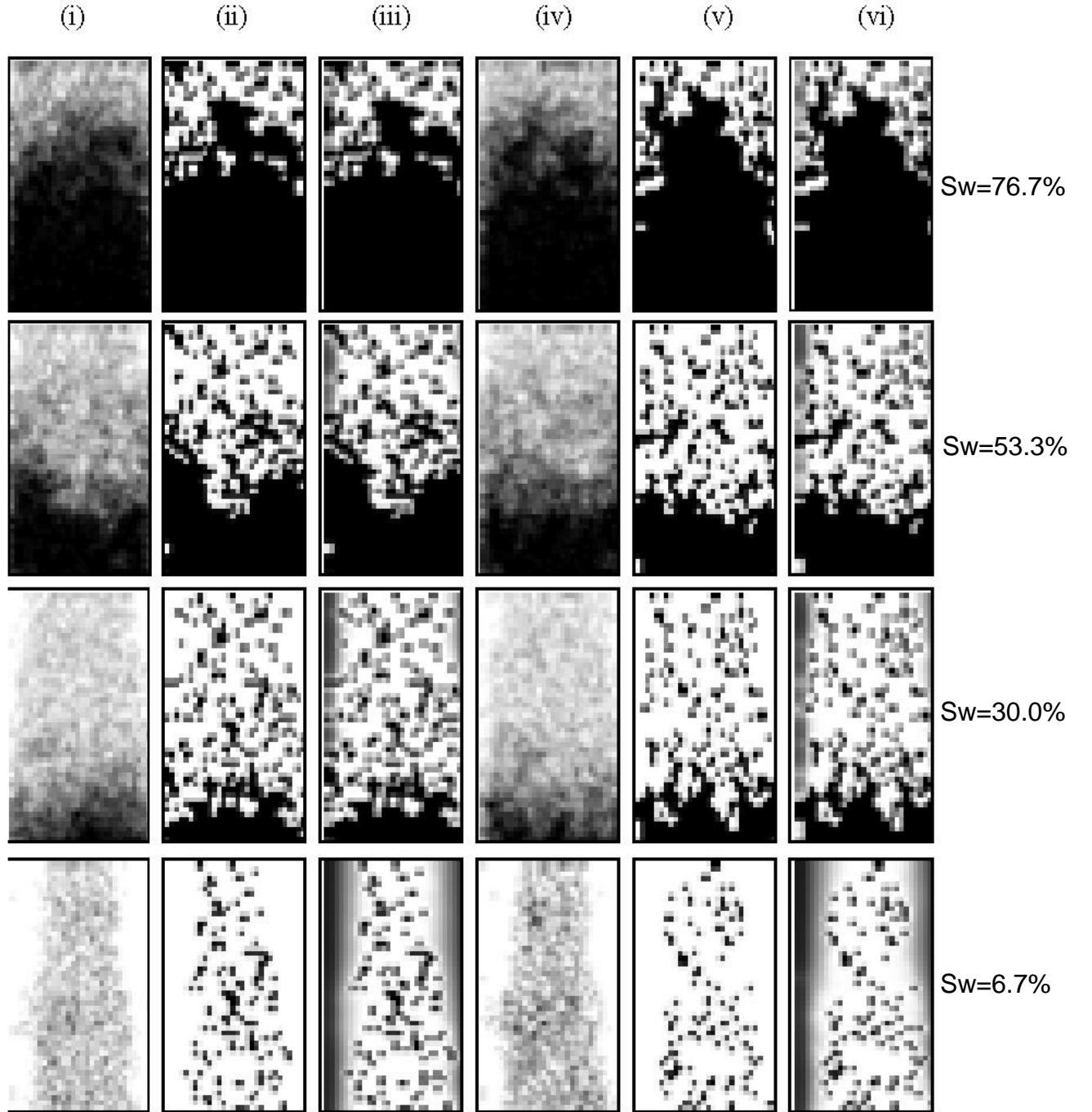
Figure 2: Drying model results for all side surfaces open and top and bottom surfaces closed. Legend as for Figure 1.
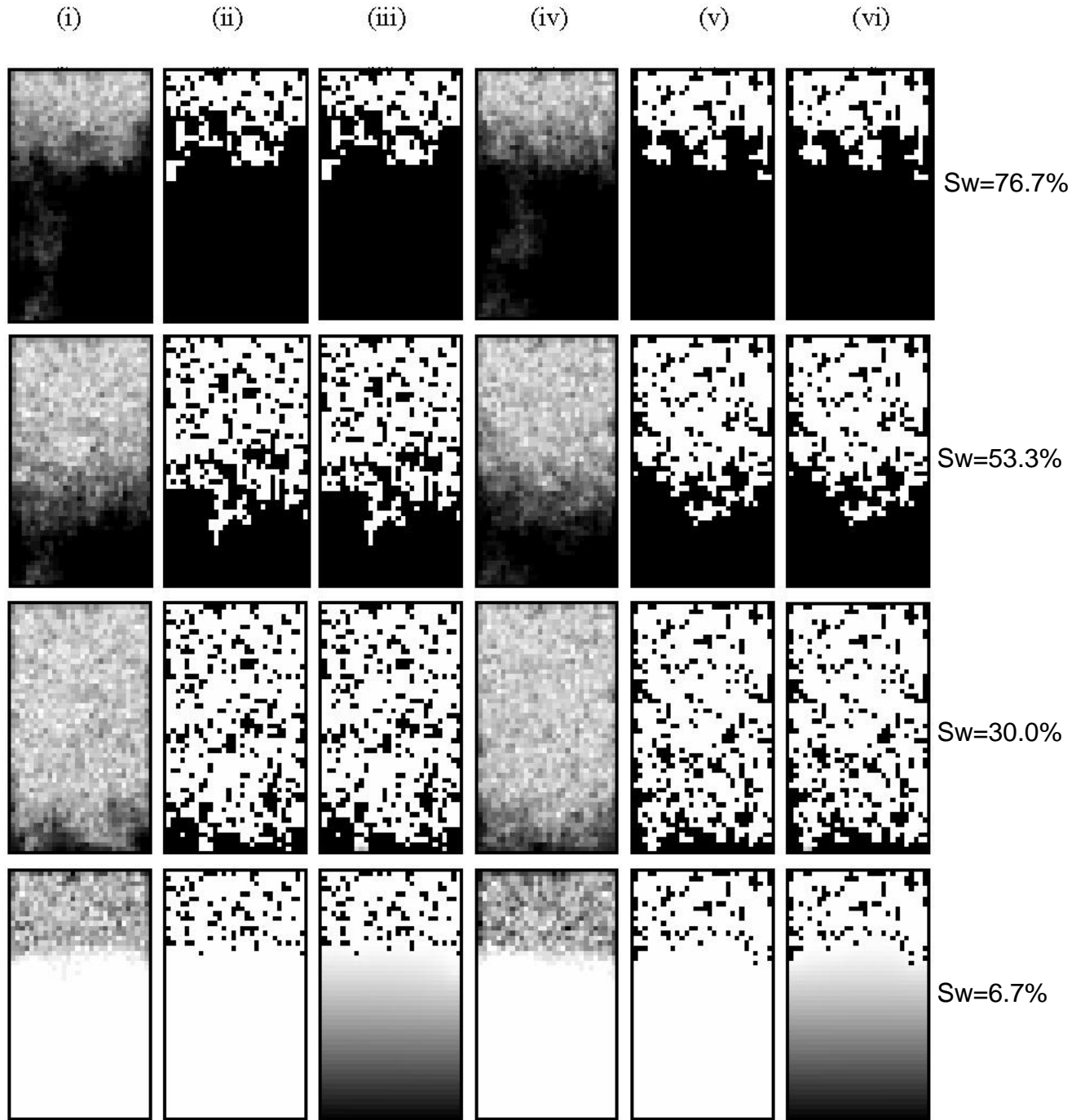
Figure 3: Drying model results for bottom surface open and all other surfaces closed. Legend as for Figure 1.
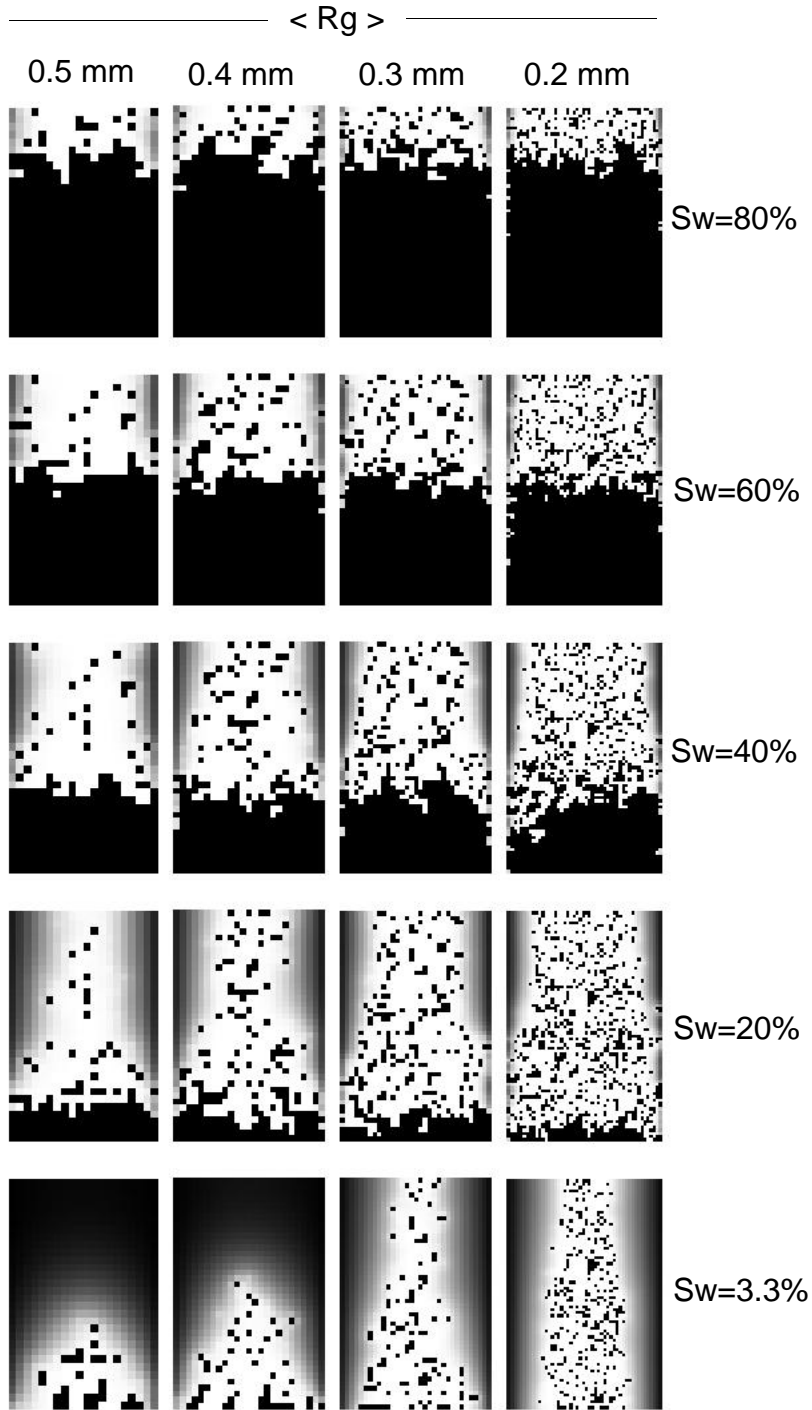
Figure 4: Phase distributions and water vapor concentration for variation in grain size, constant physical system size. Grain size decreases to the right. Each image is 2 cm × 3 cm, and water saturation decreases from top to bottom.
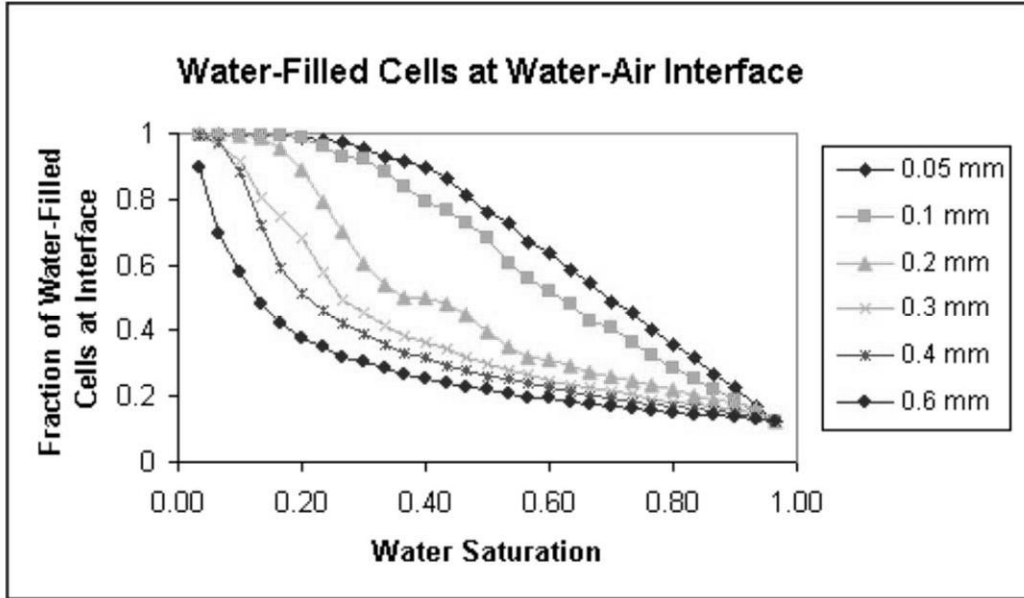
Figure 5: Variation of the fraction of water-filled cells at the air-water interface with respect to water saturation, parameterized for different grain sizes assumed in drying model.
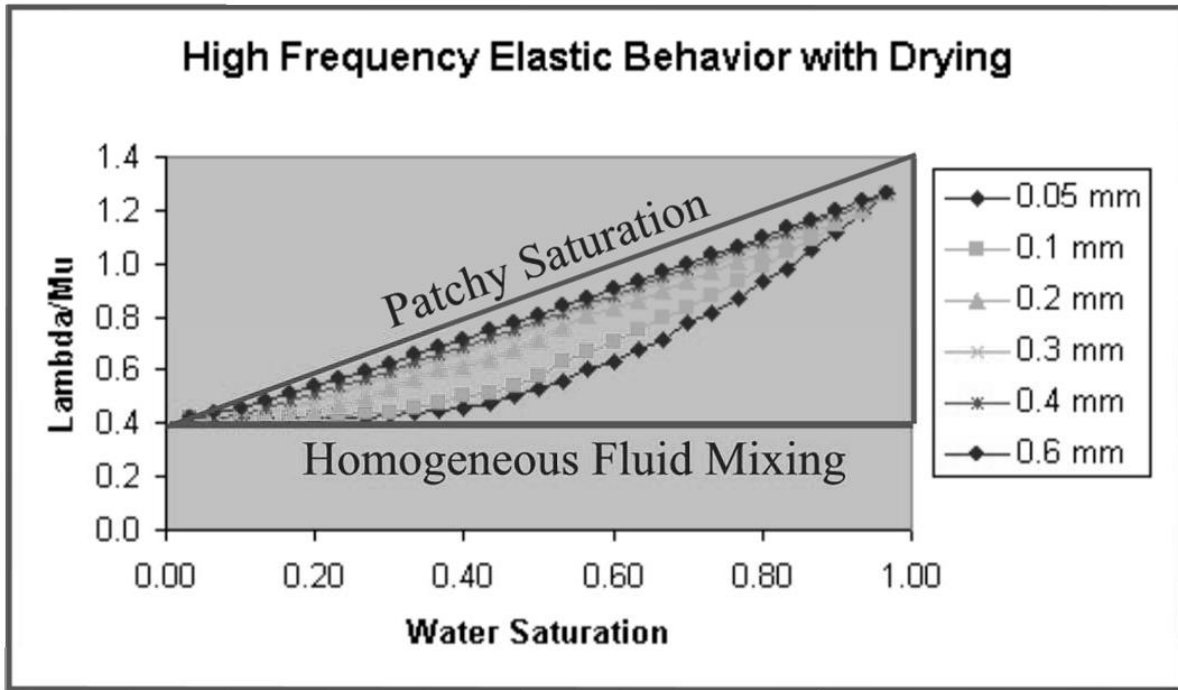

Figure 6: λ/μ versus water saturation for different average grain sizes. Base of bounding triangle is low-frequency Gassmann prediction, and hypotenuse is high-frequency prediction of ideal patchy saturation behavior [*Berryman et al.*, 2002].
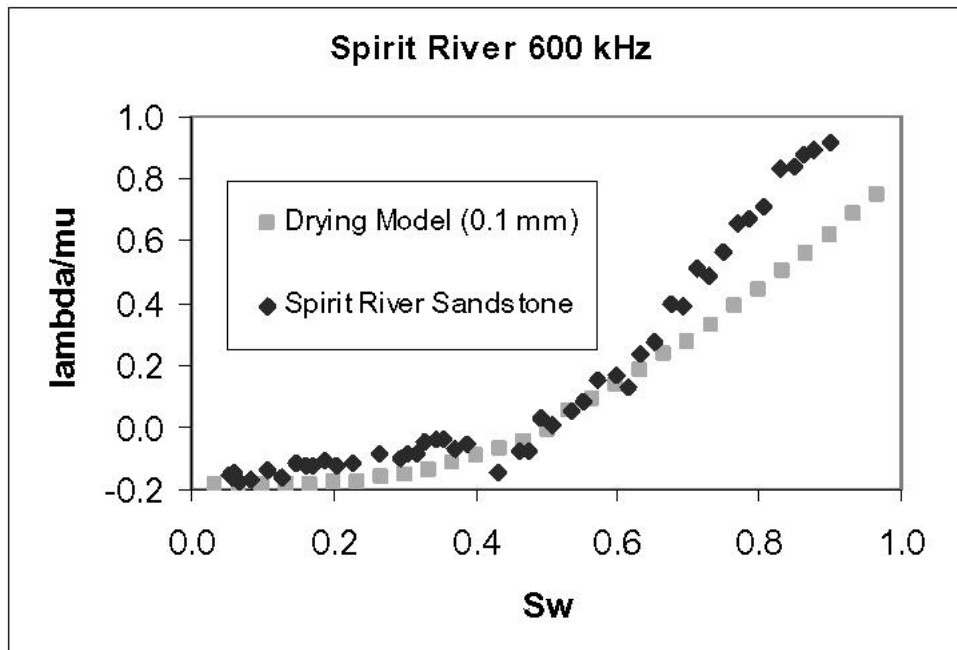
Figure 7: Sandstone data [*Knight and Nolen-Hoeksema,* 1990] superposed on drying model curves. Spirit River sandstone shows behavior intermediate between patchy and low-frequency, drained behavior.
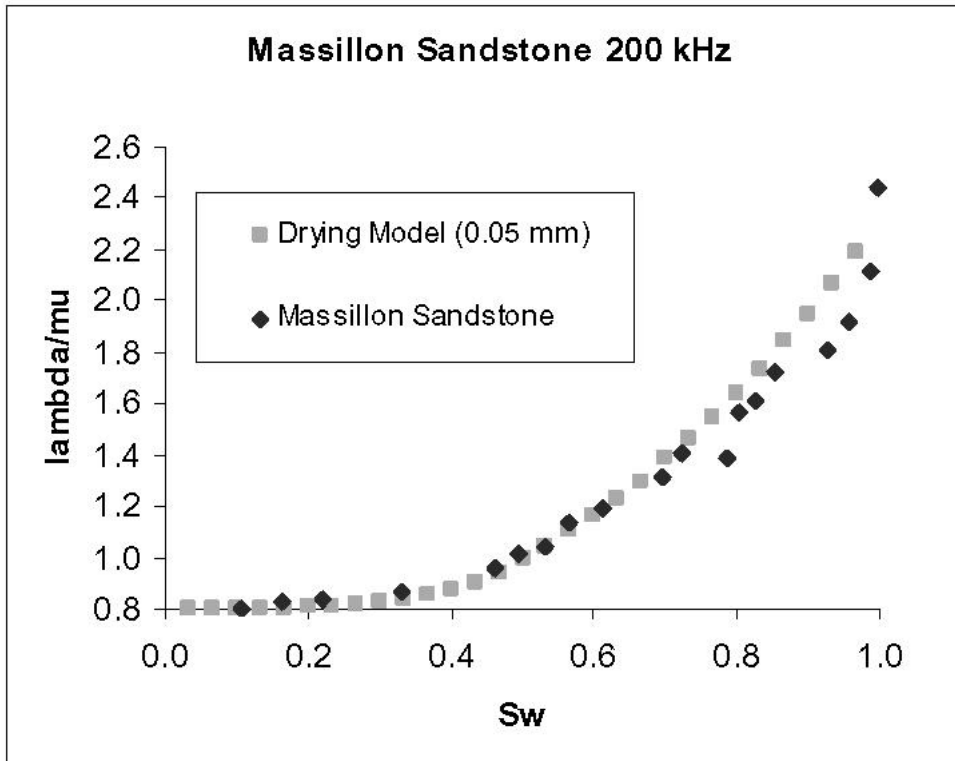
Figure 8: Sandstone data [*Murphy,* 1984] superposed on drying model curves. Massillon sandstone shows behavior intermediate between patchy and low-frequency, drained behavior.
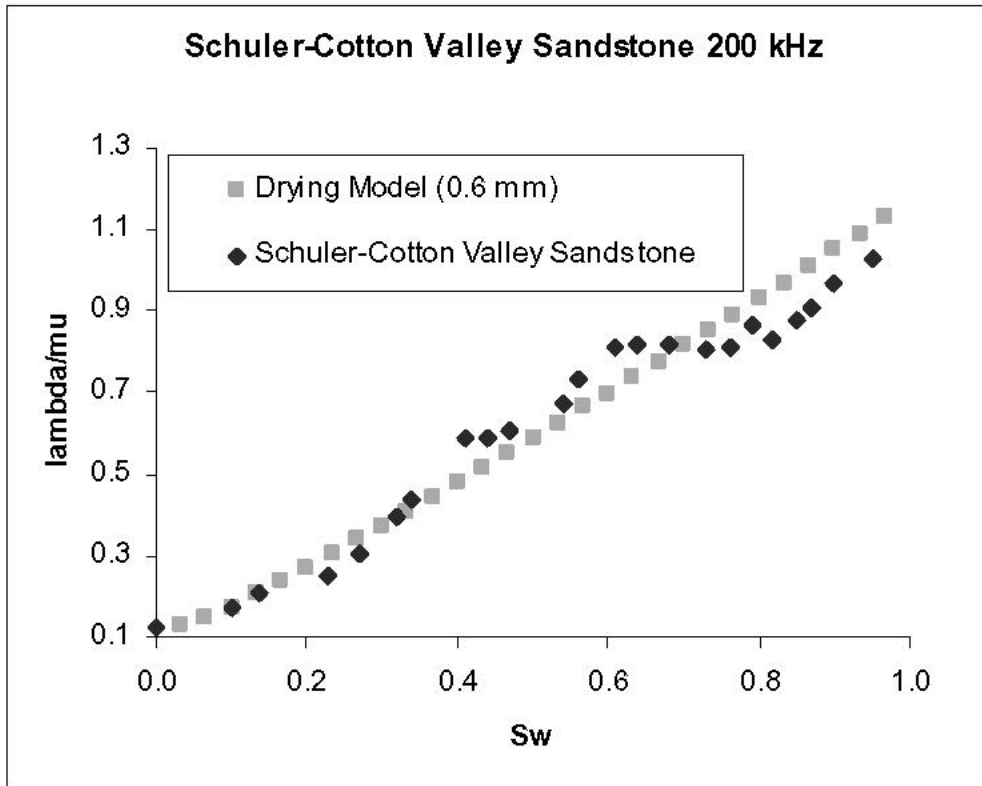
Figure 9: Sandstone data [*Murphy,* 1984] superposed on drying model curves. Schuler-Cotton Valley sandstone shows ideal patchy behavior.